Environmental Science: Atmospheres

ROYAL SOCIETY OF CHEMISTRY

PAPER

View Article Online
View Journal | View Issue

Cite this: *Environ. Sci.: Atmos.*, 2023, **3**, 1767

Assessing the atmospheric fate of trifluoroacetaldehyde (CF_3CHO) and its potential as a new source of fluoroform (HFC-23) using the AtChem2 box model†

Maria Paula Pérez-Peña, *[a] Jenny A. Fisher, *[b] Christopher Hansen [a] and Scott H. Kable [a]

The use of human-made refrigerants and blowing agents have a long record of restrictions because of the impacts their emissions have had on atmospheric composition and climate. One of the most recent alternatives for replacing some of the harmful and banned refrigerants and blowing agents is hydrofluoroolefins (HFOs). An example is HFO-1234ze, proposed as a replacement for HCFC-141b in the polyurethane foam industry. HFO-1234ze reacts almost exclusively with OH to produce formyl fluoride (HFCO) and trifluoroacetaldehyde (CF_3CHO). However, the photodissociation of CF_3CHO to fluoroform (CHF_3 or HFC-23) has been shown to be a possible channel. Although the HFC-23 channel quantum yield is reported to be small (~0.3%), this channel needs to be characterised because HFC-23 is a long-lived gas with a 100-year global warming potential (GWP-100) of 12 690. In this study, we use a suite of AtChem2 box model simulations to determine how CF_3CHO is lost in the atmosphere and how much HFC-23 can be produced from its photolysis under realistic atmospheric conditions. We tested a range of scenarios with varying HFO-1234ze emission rates and HFC-23 quantum yields. We also accounted for the physical removal of CF_3CHO by obtaining a range of deposition rates using the GEOS-Chem 3-D chemical transport model. We find that over one month, an upper value of 0.31 ppt of HFC-23 could be produced from HFO-1234ze through CF_3CHO photolysis. Globally, the HFC-23 photolysis channel explored here could be responsible for ~4–15% of the current HFC-23 growth rate.

Received 1st August 2023
Accepted 20th October 2023

DOI: 10.1039/d3ea00120b

rsc.li/esatmospheres

Environmental significance

The atmospheric degradation of HFO-1234ze (1,1,1,3-tetrafluoropropene), a fourth-generation refrigerant, leads to the production of fluoral (CF_3CHO). Photolysis of fluoral has been reported to produce a small amount of HFC-23 (trifluoromethane, or fluoroform) as a photolysis product with a quantum yield that is strongly pressure dependent.[3] HFC-23 is one of the most potent greenhouse gases with a global warming potential of 12 690 over 100 years. We conducted atmospheric box modelling of HFO-1234ze at two scales and quantified the various degradation pathways under 14 different modelling scenarios. The model predicts that HFC-23 formed from this mechanism may reach 0.3 ppt over China (2.6 ppq globally) and contribute to 4–15% of the annual increase of HFC-23 in the atmosphere.

1 Introduction

The widespread use of halogenated industrial gases for refrigeration, heat pumps, foam blowing agents and other uses started in the 1930s as replacements for naturally occurring gases that were toxic, flammable and explosive. Their consequent impact on the ozone layer and then as greenhouse gases (GHGs) led to the constant iteration of their chemical structure and properties to minimise the impact on Earth's atmosphere, while retaining their important use in society. Previous works have extensively detailed the evolution of halogenated industrial gases.[4–7] The diagram in Fig. 1 shows the progression of these substances, and also the regulations that have been put in place dictating their evolution. The pursuit to develop and use refrigerants and blowing agents that have no ozone depleting potential (ODP) and a negligible global warming potential (GWP) (currently GWP <150 in the European Union[6]) has paved the way for a fourth generation of refrigerants.

One family of substances that have the right physical properties as refrigerant gases and fulfill the requirement of zero ODP and low GWP are the hydrofluoroolefins (HFOs). HFOs

[a]*School of Chemistry, University of New South Wales, Sydney, NSW, Australia. E-mail: mpperezpena@hotmail.com*

[b]*Centre for Atmospheric Chemistry, School of Earth, Atmospheric and Life Sciences, University of Wollongong, Wollongong, NSW, Australia. E-mail: jennyf@uow.edu.au*

† Electronic supplementary information (ESI) available. See DOI: https://doi.org/10.1039/d3ea00120b

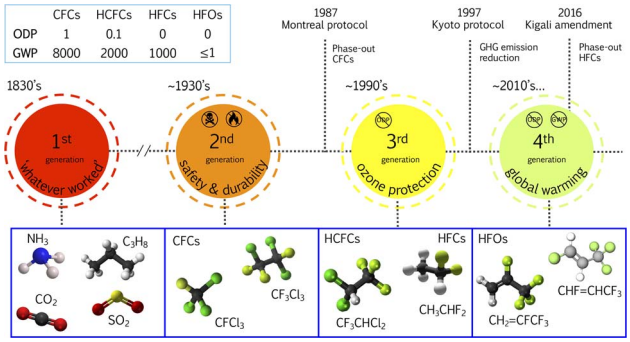

Fig. 1 Evolution of refrigerant gases including some example molecules, as well as the years in which they started to be used and corresponding years when important protocols and amendments took place. The values for the ozone depleting potential (ODP) and global warming potential (GWP) are reference values only; for specific molecules, the ODP and GWP can be higher or lower. Adapted from Calm,[5] McLinden and Huber,[6] Park *et al.*[7]

possess a carbon–carbon double bond, which is labile to attack by the hydroxyl radical (OH˙). Therefore their atmospheric lifetime is short, and they are characterized to have a low GWP. The OH radical chain reaction leads to the formation of fluorinated carbonyls and acids. For example, trifluoroacetic acid (CF_3COOH) is formed from HFO-1234yf ($CF_3CF{=}CH_2$).[8] Carbonyl fluoride (FCFO) and trifluoroacetaldehyde (CF_3CHO) are formed from HFO-1234ze ($CF_3CH{=}CHF$),[9] HFO-1336mzz ($CF_3CH{=}CHCF_3$)[10] and HCFO-1233zd ($CF_3CH{=}CHCl$).[11]

The environmental impact of HFOs is inextricably linked with the environmental impact of their decomposition products. Trifluoroacetic acid (TFA) is highly soluble and removed rapidly from the atmosphere; however, it is persistent in the aquatic environment and has been detected in rivers, oceans, plants that form part of the food chain, and food products.[12] As a result, in early 2023, the European Chemicals Agency published a proposal to ban TFA and its precursors, including some HFOs. Trifluoroacetaldehyde, on the other hand, both photolyses and reacts with OH radicals in the atmosphere. It is not a likely to be a persistent substance. Its principal decomposition pathways produce FCHO, which is considered environmentally benign because it is readily hydrolysed. However, recent work in our group has demonstrated a small, but measurable, pressure-dependent quantum yield of HFC-23 in its photolysis.[3]

HFC-23 has a very high global warming potential (GWP_{100} of 12 690) and a long atmospheric lifetime (228 years).[13,14] The current HFC-23 in the atmosphere comes mostly from its emission as a by-product of HCFC-22 (CHF_2Cl) manufacturing, with additional sources from its use in halon-1301 (CF_3Br) production, the semiconductor industry and fire extinguishers.[13,15] Despite slowdowns in the production of HCFC-22 and the introduction of HFC-23 abatement technologies in response to the Kigali Amendment to the Montreal Protocol, observations show atmospheric HFC-23 has continued to increase in recent years, with a growth rate of ~1 ppt per year.[13,16] This discrepancy has primarily been attributed to under-reported HCFC-22 production and/or unsuccessful implementation of abatement policies. Here, we explore the potential additional contribution to HFC-23 growth from photolytic production associated with growing emissions of HFOs.

In this research, we seek to understand the atmospheric fate of CF_3CHO by using atmospheric modeling. We use HFO-1234ze as an exemplar precursor because it is in widespread commercial use and there is a recent study providing estimates of both present-day emissions and emission projections.[1] HFO-1234ze is proposed as a replacement for the hydrochlorofluorocarbon HCFC-141b in the foam industry,[1] so its use is expected to increase as HCFC-141b is supposed to be completely phased out by 2030. To describe the fate of CF_3CHO produced from HFO-1234ze, we first review CF_3CHO sources, chemistry and loss processes.

1.1 Sources and sinks of HFO-1234ze and CF_3CHO

The proposed chemical reaction pathway for HFO-1234ze with the OH radical is shown in Fig. 2. OH˙ can add to either side of the double bond giving two branched pathways. However, following reaction with O_2 and NO, two carbonyls are formed from either branch: CHFO and CF_3CHO. The yield of these products is 100% from the HFO.[9] Because CF_3CHO is the link between the HFO-1234ze and HFC-23, it is important to characterize its sources and sinks.

CF_3CHO, also known as trifluoroacetaldehyde or fluoral, is a fluorinated, non-naturally-occurring compound. The main chemical sinks in the atmosphere are the reaction with OH˙ and photolysis following absorption of solar radiation. Two photolysis pathways have been reported in the literature.[17] It is widely accepted that the main photolysis channel for CF_3CHO produces formyl (HCO˙) and trifluoromethyl (CF_3˙) radicals (reaction (1)). The second, minor photolysis channel produces fluoroform HFC-23 (CHF_3) and CO (reaction (2)).

$$CF_3CHO + h\nu \rightarrow {}^{\cdot}CF_3 + HCO^{\cdot} \quad (1)$$

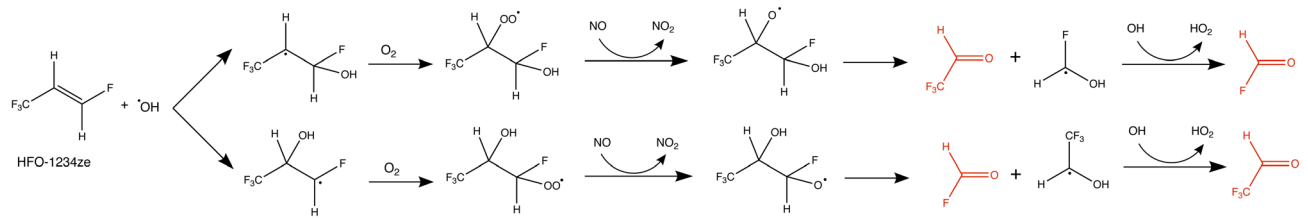

Fig. 2 Proposed decomposition pathway of HFO-1234ze following reaction with OH˙ leading to CF_3CHO and CHFO production.[9] The produced CF_3CHO is highlighted in red.

$$CF_3CHO + h\nu \rightarrow CHF_3 + CO \quad (2)$$

The OH˙ radical extracts the aldehyde H-atom to produce the trifluoroacetyl radical, $CF_3CO^{\bullet}$, and water, with a rate coefficient of 6.3×10^{-13} cm^3 molec^{-1} s^{-1}.[1]

$$CF_3CHO + {}^{\bullet}OH \rightarrow CF_3CO^{\bullet} + H_2O \quad (3)$$

Chiappero *et al.*[17] measured a total photolysis quantum yield for CF_3CHO at 308 nm and atmospheric pressure to be $\phi_{tot} = 17\%$. Sulbaek Andersen *et al.* focused on measuring a quantum yield for the formation of HFC-23 (reaction (2)). They did not successfully measure HFC-23, and inferred an upper limit for the quantum yield to be $\phi_2 = 0.3\%$.[2] Chiappero *et al.*[17] reached a similar conclusion, suggesting that the contribution of fluorinated aldehyde photolysis, including CF_3CHO, to HFC-23 formation was of small significance.

Recently, HFC-23 was directly measured in a series of experiments at different pressures, albeit at pressures lower than in the troposphere.[3] At zero pressure, the quantum yield of HFC-23 at 308 nm photolysis was measured to be $\phi_2(0\ \text{bar}) = 15\%$. Reaction (2), however, was strongly quenched. At 4 Torr of helium, ϕ_2 dropped to 7% and further to 1.5% at 33 Torr pressure of NO radical scavenger. The extrapolated quantum yield at 1 bar pressure was estimated to be ≈1%.

In terms of the physical sinks of CF_3CHO, there is no information regarding whether and how the species is likely to deposit. There are no reported values for the dry deposition velocity. Likewise, CF_3CHO wet deposition has never been reported, and although it can be estimated using existing parameterizations, the required Henry's law constants are not well characterized for CF_3CHO. Both dry and wet deposition of CF_3CHO are further explored in this work.

2 Experimental design and model development

To model the atmospheric fate of CF_3CHO, we used the AtChem2 v1.2.1 box model implementing the Master Chemical Mechanism (MCMv3.3.1). We implemented the box model to describe a simplified representation of the global planetary boundary layer. The following sections detail the model input parameters, including the chemical mechanism (Section 2.1), HFO-1234ze emissions (Section 2.2), CF_3CHO deposition (Section 2.3), and the chemical and meteorological constraints used to represent realistic atmospheric conditions (Section 2.4). Finally, we describe our suite of model scenarios for simulation of CF_3CHO (Section 2.5).

2.1 Chemical mechanism

We used the MCMv3.3.1 chemical mechanism and extracted two subsets, one representing an urban atmosphere (including 11 667 reactions) and a second representing a pristine atmosphere (including 2753 reactions).[18,19] In both cases, the standard MCMv3.3.1 mechanism was augmented with five new reactions and seven new species: HFO-1234ze, CF_3CHO, CHFO, HFC-23, $HCO^{\bullet}$, $CF_3^{\bullet}$ and $CF_3CO^{\bullet}$. Table 1 lists the new reactions along with the relevant reaction rate coefficients and quantum yields.

Table 1 New reactions and corresponding rate coefficients (k) and quantum yields (ϕ) added to MCMv3.3.1 in this work

Reaction	k [cm^3 molec^{-1} s^{-1}]	ϕ [%]
HFO-1234ze + OH˙ → CF_3CHO + CHFO	1.00×10^{-12}[a]	
CF_3CHO + OH˙ → CF_3CO + H_2O	6.50×10^{-13}[a]	
$CF_3CHO + h\nu \rightarrow CHF_3 + CO$		0.3[b], 1.0[c]
$CF_3CHO + h\nu \rightarrow CF_3^{\bullet} + HCO^{\bullet}$		16.7, 16.0[d]
$CHF_3 + OH^{\bullet} \rightarrow CF_3^{\bullet} + H_2O$	3.10×10^{-16}[e]	

[a] Wang *et al.*[1] [b] Sulbaek Andersen and Nielsen.[2] [c] Campbell.[3] [d] Calculated as the difference between the overall quantum yield of 17% from Chiappero *et al.*[17] and the value used for the HFC-23 channel. [e] Sander *et al.*[20]

The quantum yields for CF_3CHO photolysis were treated as variables in this work. Guided by the experiments of Chiappero *et al.*,[17] we fixed $\phi_{tot} = 17\%$. We tested two quantum yields for the HFC-23 channel (reaction (2)). $\phi_2 = 0.3\%$ was chosen to reflect the values in the Sulbaek Andersen[2] paper, reported as an upper limit at 1 bar. $\phi_2 = 1\%$ was the extrapolated value by Campbell[3] and chosen to reflect a realistic upper bound. The quantum yield for the radical channel (ϕ_1) was assumed to be $\phi_{tot} - \phi_2$, *i.e.,* 16.7% and 16%, respectively. We did not include pressure dependence in the quantum yields. To calculate the photolysis rates, we used CF_3CHO absorption cross sections from 200–400 nm at 298 K reported by Sellevag *et al.*[21] (see Fig. S1†) and actinic flux values from Petterson.[22]

2.2 Emissions of HFO-1234ze

We used HFO-1234ze emissions projections from Wang *et al.*[1] of 12.6 Gg per year for 2015 and 124.4 Gg per year for 2050, with the former the only data currently available for present-day HFO-1234ze emission estimates. We assumed emissions are well-mixed throughout the planetary boundary layer (PBL), with average PBL depth of 2 km. For each emission year, we considered two scenarios: one in which the Wang *et al.*[1] emissions were distributed globally and a second in which emissions were concentrated over China. The former provides a simulation representative of the global background, while the latter represents the localised impact over China (the dominant HFO-1234ze source globally and sole source considered by Wang *et al.*[1]). In all cases, the HFO-1234ze emission rate was constant throughout the simulation.

2.3 Dry and wet deposition of CF_3CHO

The deposition process in AtChem2 defines a single deposition flux F (in molecules cm^{-2} s^{-1}) as shown in eqn (4):[23]

$$F = V_{dep} \times C \quad (4)$$

where V_{dep} is the deposition velocity in cm s^{-1} and C is the concentration of the species of interest in molecule cm^{-3}. The

parsimonious physical approach employed by AtChem2 allows for only a single deposition flux, which we use here to represent both dry and wet deposition processes (dominated by dry deposition, as we will show below).

To the best of our knowledge, there are no existing measurements or estimates of CF_3CHO deposition fluxes or the parameters required to calculate them. Here we estimate deposition rates using deposition parameterizations in the GEOS-Chem chemical transport model v12.5.0 (doi: 10.5281/zenodo.3403111), with a modified version of acetaldehyde (CH_3CHO) used as a proxy for CF_3CHO.

For dry deposition, GEOS-Chem calculates a deposition velocity that can be applied directly in AtChem2 using eqn (4). For wet deposition, on the other hand, the GEOS-Chem algorithm does not involve calculation of an equivalent rate. For application to AtChem2, we instead use the ratio of wet to dry deposition fluxes from GEOS-Chem to approximate the relationship between wet and dry deposition and scale the dry deposition velocity by this ratio. In the next sections, we briefly describe the parameters used to simulate these processes for CF_3CHO and the process used to determine the most appropriate overall deposition velocity to use in our AtChem2 simulations.

2.3.1 Dry and wet deposition parameters. To calculate the dry deposition velocity (cm s^{-1}), GEOS-Chem incorporates a resistance-in-series scheme[24] that depends on species-specific values for the Henry's law solubility constant, H^{cp} (M atm^{-1}), and the reactivity factor for oxidation of biological substances, f_0 (unitless).

Two compendiums of Henry's law constants report H^{cp} for CF_3CHO. A 1989 report on the lifetimes of HFCs and HCFCs[25] suggested values of $H^{cp}(CF_3CHO)$ between 10^5 M atm^{-1} and 10^6 M atm^{-1}. However, the original source cited by the report[26] does not include measurements for CF_3CHO, but rather for its chlorinated equivalent, chloral (CCl_3CHO). It is not clear on what basis it was determined that the H^{cp} of CF_3CHO would be equivalent to that of CCl_3CHO. A more recent review[27] reports the CF_3CHO H^{cp} to range between 0.96 M atm^{-1} and 3 M atm^{-1}. In this case, the original source cited for these values is de Bruyn *et al.*,[28] who also did not directly study CF_3CHO but rather performed gas–liquid uptake studies on trifluoroacetyl fluoride (CF_3CFO). It is unclear whether CF_3CHO has a comparable solubility to CF_3CFO, and no information is provided in either source to explain why both gases would have the same H^{cp}. To the best of our knowledge, no other sources report CF_3CHO H^{cp} measurements.

To explore appropriate analogues for CF_3CHO H^{cp}, we investigate the relationship between H^{cp} for various small, oxygenated organic species and the effect of fluorination. Table S1† compares several properties, including H^{cp}, for a set of small aldehydes, ketones, ethers and esters. Species that dissociate in solution, for example acids, are excluded. Table S1† shows that the H^{cp} values of fluorinated compounds are consistently one to two orders of magnitude smaller than their hydrogenated counterparts. For species where H^{cp} is reported for different degrees of fluorine substitution, increasing F-substitution leads to lower H^{cp}. In this regard, we consider $H^{cp}(CF_3CHO)$ very likely to lie between the reported values for $H^{cp}(CH_3CHO) = 13.2$ M atm^{-1} and $H^{cp}(CF_3CFO) = 0.96$ to 3.0 M atm^{-1}. In this study, we test the sensitivity to this parameter, using these values as upper and lower bounds of H^{cp} for CF_3CHO. Given the data in Table S1,† we believe the value of $H^{cp}(CF_3CHO)$ is likely to be near the upper range for CF_3CFO = 3 M atm^{-1}.

The reactivity factor, sometimes called the biological reactivity factor, f_0, is indicative of how reactive a gaseous species is within a plant,[24] ranging between $f_0 = 0$ for a non-reactive gas like SO_2 and $f_0 = 1$ for a highly reactive gas, such as O_3. In GEOS-Chem, acetaldehyde is considered a highly reactive gas with reactivity factor $f_0 = 1$. The reactivity factor for CF_3CHO is unknown. Here we bracket the range of possibilities (and test the sensitivity to this parameter) using $f_0 = 0$ as a lower bound and $f_0 = 1$ as an upper bound.

The wet deposition scheme in GEOS-Chem is described by Liu *et al.*[29] The calculation requires species-specific values for the temperature dependence of H^{cp} $\left(\frac{d \ln H^{cp}}{d(1/T)}\right)$. We did not find any published estimates for $\frac{d \ln H^{cp}}{d(1/T)}$ for CF_3CHO. Table S1† shows that $\frac{d \ln H^{cp}}{d(1/T)}$ for all compounds, both hydrogenated and fluorinated, lies within about a factor of two range (3900 to 8900 K in the table) with no clear trend. The determination of $\frac{d \ln H^{cp}}{d(1/T)}$ for a given species requires knowledge of the enthalpy of dissolution ($\Delta_{sol}H$),[30] a value that to the best of our knowledge is not known for CF_3CHO. Without further constraints, we used the value for acetaldehyde of $\frac{d \ln H^{cp}}{d(1/T)} = 5900$ K, which lies in the middle for the range of compounds,[30] as the best available proxy for CF_3CHO.

2.3.2 CF_3CHO deposition rate estimates. We used the parameters described above as inputs for a deposition-only simulation in the GEOS-Chem model. We based our CF_3CHO simulation on the existing simulation for acetaldehyde,[31] modifying physical constants (*e.g.*, molecular weight) and turning off model processes that do not apply to CF_3CHO (*e.g.*, air–sea exchange). GEOS-Chem does not include a description of CF_3CHO chemistry or precursor emissions, and so does not provide a realistic simulation of CF_3CHO. Instead, we used GEOS-Chem to provide estimates of the dry deposition velocity and the wet-to-dry deposition flux ratio to be used as inputs to AtChem2. While the deposition velocity is independent of mixing ratio, both wet and dry deposition fluxes depend on species mixing ratio; here, we use the ratio between these to minimise this impact (although this remains an uncertainty). We set the initial condition for CF_3CHO mixing ratio to 2.5 ppt in all grid boxes, guided by the average global mixing ratio modelled by Wang *et al.*[1].

We ran GEOS-Chem driven by Goddard Earth Observing System Forward Processing (GEOS-FP) meteorology from the Global Modeling and Assimilation Office (GMAO) meteorology at coarse resolution (4° × 5° × 72 levels) for January and June 2014 to capture seasonal variability in deposition rates and

fluxes. We output daily average deposition values for CF_3CHO, as well as for acetaldehyde to test our approach. Results for acetaldehyde can be found in the ESI Material and Fig. S2.†

Fig. 3 shows the dry deposition velocities for CF_3CHO for June 2014 modelled using the upper and lower estimates for H^{cp} and $f_0 = 1$. Fig. S3† shows the equivalent results for January 2014. The choice of f_0 had no impact on any of our simulations and we do not discuss it further. With $H^{cp} = 0.96$ M atm^{-1}, the global maximum CF_3CHO dry deposition velocity was 0.13 cm s^{-1} in January and 0.18 cm s^{-1} in June. With the upper bound $H^{cp} = 13.17$ M atm^{-1} (from acetaldehyde), the maximum global dry deposition velocity was 0.67 cm s^{-1} in both months. Despite a factor of 13 difference in assumed H^{cp} between these two scenarios, the resulting dry deposition velocity increase was a factor of ~4, implying only moderate sensitivity to this parameter, at least within the range of plausible values examined here.

Table 2 shows the globally-averaged dry deposition velocities for each H^{cp} scenario and each month. The global mean CF_3CHO dry deposition velocity ranged between 0.007 cm s^{-1} and 0.07 cm s^{-1}, increasing with H^{cp}, with higher values in June (northern hemisphere summer) than January.

Table 2 also shows the ratio of global total wet and dry deposition fluxes (F_{wet}/F_{dry}). As seen in the table, with $H^{cp} = 0.96$ M atm^{-1}, the wet deposition flux was roughly one third the dry deposition flux in January and one fifth the dry deposition flux in June. The relative importance of the wet deposition flux decreased with increasing H^{cp}. In all scenarios, wet deposition made a relatively small contribution to the overall CF_3CHO deposition flux (~8–25%).

Based on these results, we chose upper and lower values of total V_{dep} (representing both dry and wet deposition processes) to use in AtChem2 for each of our two emission scenarios (see Section 2.2). We used the June results for consistency with our meteorological constraints for northern hemisphere summer (see Section 2.4). For the global emission scenario, we used the global average V_{dep} scaled by $f = 1 + F_{wet}/F_{dry}$ to account for the wet deposition contribution, resulting in lower and upper estimates for global V_{dep} of 0.02 cm s^{-1} and 0.08 cm s^{-1}, respectively. For the China-only emission scenario, we retained the same lower value but replaced the upper value with the June maximum dry deposition velocity from the $H^{cp} = 0.96$ M atm^{-1} simulation ($V_{dep} = 0.18$ cm s^{-1}), again scaled by the wet deposition contribution, for an overall $V_{dep} = 0.21$ cm s^{-1}. The latter is used to represent the maximum plausible contribution of deposition to CF_3CHO removal over a continental surface.

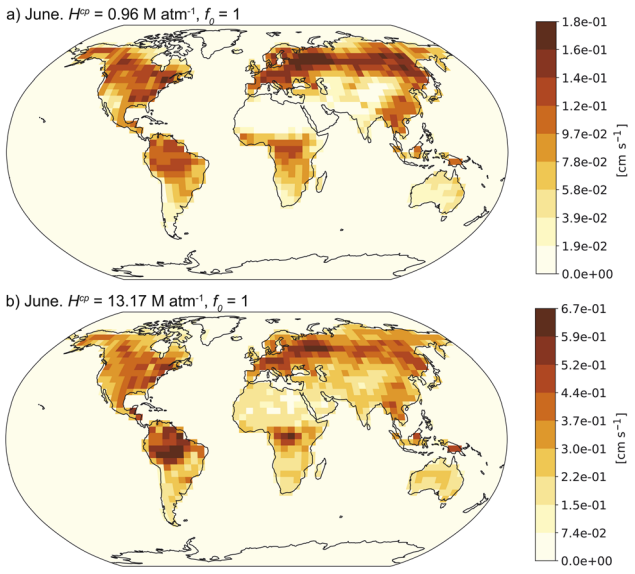

Fig. 3 Average monthly CF_3CHO dry deposition velocities simulated by GEOS-Chem for June 2014 using $f_0 = 1$ and (a) $H^{cp} = 0.96$ M atm^{-1} *versus* (b) $H^{cp} = 13.17$ M atm^{-1}.

Table 2 Average global CF_3CHO dry deposition velocities (V_d) and deposition flux ratios (F_{wet}/F_{dry}) from GEOS-Chem

Species	H^{cp} [M atm^{-1}]	f_0	Month	Mean V_d [cm s^{-1}]	F_{wet}/F_{dry}
CF_3CHO	0.96	1	Jan	0.007	0.35
CF_3CHO	0.96	1	Jun	0.02	0.21
CF_3CHO	13.17	1	Jan	0.03	0.14
CF_3CHO	13.17	1	Jun	0.07	0.09

2.4 Chemical and meteorological constraints

We constrained AtChem2 with ambient chemical and meteorological data to ensure realistic OH$^{\bullet}$ mixing ratios in our simulations. We used measurements from the May–June 2007 Cabo Verde experiment[32] to simulate pristine atmospheric conditions and from the July–August 2012 ClearfLo (Clean Air for London) measurement campaign[33] to simulate urban atmospheric conditions. From each dataset, we constructed a set of representative conditions by binning the data hourly and averaging over all measurement days for each hour (retaining the diel cycle while removing day-to-day variability). These average conditions were repeated for all days in each simulation.

2.5 Modelled scenarios

Using the parameters described in the previous sections, we designed a series of 14 scenarios to assess the atmospheric loss of CF_3CHO and the implications for HFC-23 production. For all scenarios, we simulated a 30-day period in northern hemisphere summer (sufficiently long for the model to reach steady state, as we will show later). We assumed no initial HFO-1234ze, CF_3CHO or HFC-23 to understand the evolution of all three species from a new emission source.

Table 3 summarises the model scenarios along with their corresponding identifiers. The first two scenarios (*GU15_uqy_ndep* and *GP15_uqy_ndep*) were designed to test the influence of urban *versus* pristine atmospheric conditions, influencing both the chemical mechanism (Section 2.1) and the constraints (Section 2.4). Our main interest in these scenarios was determining whether differences in OH$^{\bullet}$ between the two environments would significantly impact CF_3CHO chemical

Table 3 Scenario identifier, emissions, quantum yields (ϕ) and deposition velocities (V_{dep}) used in AtChem2 simulations

Scenario ID[a]	Year	Emission region	Emis. [Gg per year]	Radical channel ϕ_1 [%]	HFC-23 channel ϕ_2 [%]	V_{dep} [cm s^{-1}]
GU15_uqy_ndep	2015	Global	12.6	16.0	1.0	n/a
GP15_uqy_ndep	2015	Global	12.6	16.0	1.0	n/a
G15_lqy_ldep	2015	Global	12.6	16.7	0.3	0.024
G15_lqy_udep	2015	Global	12.6	16.7	0.3	0.080
G15_uqy_ldep	2015	Global	12.6	16.0	1.0	0.024
G15_uqy_udep	2015	Global	12.6	16.0	1.0	0.080
C15_lqy_udep	2015	China	12.6	16.7	0.3	0.21
C15_uqy_udep	2015	China	12.6	16.0	1.0	0.21
G50_lqy_ldep	2050	Global	124	16.7	0.3	0.024
G50_lqy_udep	2050	Global	124	16.7	0.3	0.080
G50_uqy_ldep	2050	Global	124	16.0	1.0	0.024
G50_uqy_udep	2050	Global	124	16.0	1.0	0.080
C50_lqy_udep	2050	China	124	16.7	0.3	0.21
C50_uqy_udep	2050	China	124	16.0	1.0	0.21

[a] The first letter of the Scenario ID denotes the HFO-1234ze emissions scenario (*G* for global or *C* for China). Where present, *U* denotes urban atmospheric conditions and *P* denotes pristine atmospheric conditions; if not specified, urban conditions are used. The next two digits denote emissions year 2015 or 2050. *qy* refers to the quantum yield, with the letter preceding *qy* denoting use of the lower (*l*) or upper (*u*) values for the quantum yield of the HFC-23 channel. *dep* refers to the deposition velocity, with the letter preceding *dep* denoting no deposition velocity (*n*), the lower value for deposition velocity (*l*), or the upper value for deposition velocity (*u*). The lower and upper values for each parameter are described in the text.

fate. For this experiment, we used present-day (2015) global emissions and the 1% quantum yield for the HFC-23 channel (ϕ_2). Depositional losses were not included in these scenarios as they are not relevant to questions of chemical fate. The results of this experiment showed minimal differences between urban and pristine conditions (see Section 3.1), and so we used the urban atmosphere for all subsequent scenarios as it included more constrained species.

We simulated six scenarios using present day (2015) HFO-1234ze emissions. These included four global emission scenarios (*G*) using different combinations of lower and upper values for the quantum yield of the HFC-23 channel (*lqy*, *uqy*) and for the deposition velocity (*ldep*, *udep*). We also simulated two China emission scenarios (*C*), one using the lower values for both HFC-23 quantum yield and deposition velocity (*lqy_ldep*) and one using the upper values for both parameters (*uqy_udep*). We repeated the same six scenarios using projected 2050 HFO-1234ze emissions. The 2050 scenarios assess changes to HFO-1234ze emissions only, retaining the same present-day atmospheric conditions as used in the 2015 scenarios. We do not consider natural or technological changes to climate, meteorology, land use, or emissions of other species.

3 Modelling results and discussion

The results for the 14 modelled scenarios are detailed in this section. First, we quantify the contribution of the different evaluated loss processes to the overall removal of CF_3CHO from the atmosphere (Section 3.1). Next, we discuss how the modelled species evolve during the 30-day simulation for each scenario (Section 3.2). Finally, we discuss the possible impact that the degradation of CF_3CHO could have on current and future levels of atmospheric HFC-23 (Section 3.3).

3.1 CF_3CHO sink distribution

We used the rates of destruction (*i.e.*, loss rates, in molecules cm^{-3} s^{-1}) calculated by AtChem2 to understand the relative importance of each CF_3CHO removal process. Here, we present the sink distribution using pie charts.

We first evaluated the impact of the two different atmospheric environments (urban: *GU15_uqy_ndep* and pristine: *GP15_uqy_ndep*) on the modelling of the CF_3CHO photochemical loss (*i.e.*, excluding physical sinks). Small differences in $OH^{\bullet}$ between the two scenarios are discussed in the ESI. Fig. 4 shows the contribution of each chemical sink to the total chemical loss of CF_3CHO using the urban and pristine atmospheric conditions. Despite the two scenarios being constrained by conditions measured at very different latitudes (urban: 51°N, pristine: 15°N), the chemical pathways did not change much. The loss of

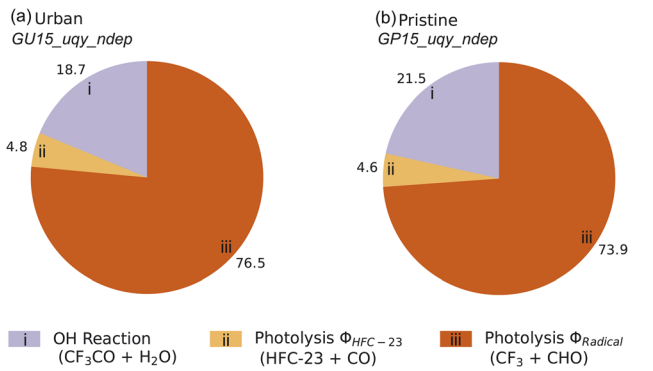

Fig. 4 Percentage contribution of each photochemical sink to the total photochemical loss of CF_3CHO for the (a) urban (*GU15_uqy_ndep*) and (b) pristine (*GP15_uqy_ndep*) scenarios, averaged over the 30-day simulation.

CF_3CHO due to reaction with OH˙ was smaller than the loss due to photolysis for both urban and pristine atmospheric settings. In both scenarios, ~4–5% of the CF_3CHO total photochemical loss was *via* the HFC-23 photolysis channel (Fig. 4).

Although the available OH˙ in the urban scenario was higher than in the pristine scenario (Fig. S4†), the CF_3CHO removal due to OH˙ was lower for the urban simulation. This may have resulted from the urban simulation including more species that react more rapidly with OH˙ than CF_3CHO, thus decreasing the OH˙ available to remove CF_3CHO. This also resulted in a slightly larger contribution of photolysis to CF_3CHO removal in the urban simulation than in the pristine simulation. Given the small differences between the two simulations, we retained only the urban conditions for all subsequent scenarios (Section 2.5).

We next evaluated the contributions of all loss processes, including deposition, to CF_3CHO removal using different combinations of model parameters. Analysis of the full suite of simulations showed the choice of emission scenario had no impact on the distribution of loss pathways, and so only the 2015 emissions scenarios (*G15* and *C15*) are discussed here.

Fig. 5 shows the contribution of each loss process for the six 2015 emissions scenarios with different ϕ_2 and V_{dep}. With the low-end values for both ϕ_2 and V_{dep} (Fig. 5a), the loss of CF_3CHO due to photolysis was 75.2%, with the majority (73.9%) removed *via* the radical channel and only 1.3% lost through the HFC-23 channel. In that scenario, reaction with OH˙ was the second most important loss process (17.5%), followed by deposition (7.3%). Increasing ϕ_2 to 1% without changing V_{dep} (Fig. 5d) did not demonstrably change the overall contributions of photolysis (75.4%), OH˙ oxidation (17.4%), and deposition (7.1%). It did, however, increase the relative importance of the HFC-23 channel to 4.4%, in direct proportion to the modelled quantum yield.

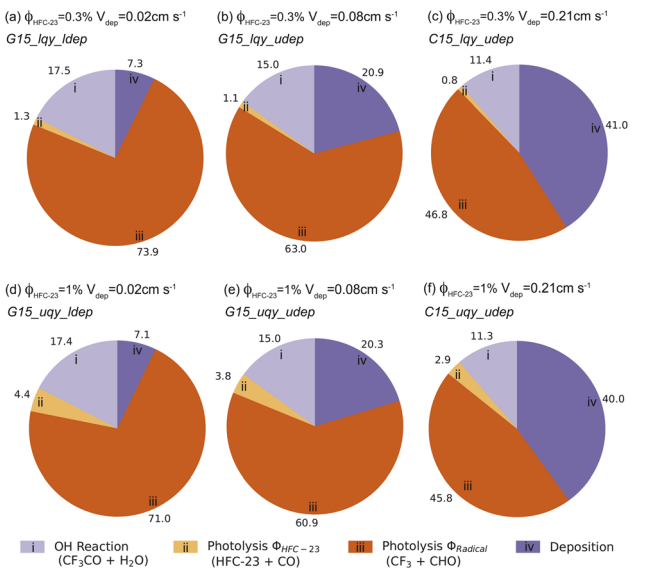

Fig. 5 Average percentage contribution of each loss process to total atmospheric removal of CF_3CHO with different deposition velocities (V_{dep}) and quantum yields for the HFC-23 channel (ϕ_2). The top panels show the *lqy* scenarios (ϕ_2 = 0.3%), and the bottom panels show the *uqy* scenarios (ϕ_2 = 1%), with increasing V_{dep} from left to right as indicated in the subtitles. All outputs are from the *G15* (a, b, d and e) or *C15* (c and f) 2015 emission scenarios as discussed in the text.

Increasing V_{dep} to the global scenario upper estimate of 0.08 cm s^{-1} (see Section 2.3.2) increased CF_3CHO deposition sufficiently to make deposition the second most important sink at ~20% (Fig. 5b and e), overtaking OH˙ oxidation (15%). Photolysis remained the dominant sink in these scenarios. Fractional loss to the HFC-23 channel was similar to that seen in the lower V_{dep} scenarios and again scaled proportionally with ϕ_2 (1.1% at ϕ_2 = 0.3%; 3.8% at ϕ_2 = 1%).

By further increasing V_{dep} in the China-only scenarios (see Section 2.3.2), we found a maximum plausible depositional loss of ~40% (Fig. 5c and f). Even in this high-deposition scenario, photolysis was the dominant loss pathway, although in this case it accounted for less than half of total CF_3CHO removal (~45%). The fractional loss to the HFC-23 channel was reduced commensurately to 0.8% with ϕ_2 = 0.3% and 2.9% with ϕ_2 = 1%.

There are two important observations to note in the data shown in Fig. 5. The first is that we find a scale factor of 2.8–4.4 between the HFC-23 atmospheric molar yield and the HFC-23 quantum yield over the course of the 30-day simulation. The scale factor is largest when other CF_3CHO removal rates are slowest (smaller V_{dep}).

The second is that the modelled atmospheric yield of HFC-23 scales linearly with modelled quantum yield. In all scenarios, the HFC-23 atmospheric yield at ϕ_2 = 1% was 3.3× the atmospheric yield at ϕ_2 = 0.3%, regardless of V_{dep}. The implication is that the HFC-23 atmospheric yield is linear with quantum yield, at least in the range $\phi_2 \in [0, 1]$%. This relationship can be used to provide an updated estimate of HFC-23 production if other experimental quantum yield measurements become available in the future. In keeping with the first observation, the atmospheric yield of HFC-23 from CF_3CHO photolysis estimated here is 2.8–4.4 × ϕ_2.

The absolute values of the CF_3CHO sinks are shown as average diel profiles in Fig. S5† for three of the global emission scenarios. The deposition sink responds to the collapse and growth of the boundary layer, peaking from late evening through early morning when the boundary layer is shallowest. Chemical sinks are negligible at these hours due to the dependence on solar radiation for both photolysis and OH˙ production. Meanwhile, the photolysis peak dominates during sunlit hours. In the simulations that used the low-end value for V_{dep} (*G15_lqy_ldep*, *G15_uqy_ldep*), the peak daytime value of the photolytic loss was significantly higher than the peak nighttime value of the depositional loss. The situation was reversed when the high-end V_{dep} was used (*G15_lqy_udep*).

We note that our simulations represent northern hemisphere summer conditions, and the CF_3CHO sinks described here could vary seasonally. Estimated dry deposition velocities were lower in January than in June by a factor of 2–3 (see Table 2). Even after taking into account the higher fractional contribution of wet deposition in January (Table 2), the overall deposition flux would be lower in winter in all modelled scenarios. At the same time, the photochemical sinks would

also be lower in winter due to reduced solar radiation. We therefore expect that, while the absolute values may vary, the relative contributions of different sink processes shown here are likely to be broadly representative.

The likelihood that the deposition process is as important as shown here is tied to the uncertainties in the underlying parameters. Not all scenarios modelled here are equally plausible, and the importance of deposition to total loss is probably overestimated. When selecting parameter values to estimate CF_3CHO deposition rates, we considered the acetaldehyde $H^{cp} = 13.17$ M atm^{-1}, and the subsequent global average deposition value $V_{dep} = 0.08$ cm s^{-1}, to be an unlikely upper limit (see Section 2.3.1). Thus, the >20% contribution of deposition to CF_3CHO loss in these scenarios is considered an unlikely global upper limit as well. The deposition contribution is more likely closer to the 7% obtained using $H^{cp} = 0.96$ M atm^{-1} ($V_{dep} = 0.02$ cm s^{-1}) (Fig. 5a and d). However, without measurements of the CF_3CHO H^{cp}, the true strength of this sink remains uncertain. We emphasize the need for measurements of CF_3CHO physical properties in future studies.

3.2 Temporal evolution of HFO-1234ze, CF_3CHO, and HFC-23

Fig. 6 shows the 30-day timeseries of HFO-1234ze, CF_3CHO and HFC-23 mixing ratios simulated using the *G15_lqy* scenarios. All other simulations showed the same behaviour but with different magnitudes (consistent with the differences in emissions). The figure shows that the AtChem2 model reached steady state for both HFO-1234ze and CF_3CHO, consistent with their estimated lifetimes of ~16 days[1] and <5 days,[17] respectively. Both species showed diel variability, driven by OH$^\bullet$ for HFO-1234ze and by a combination of OH$^\bullet$, photolysis, and deposition for CF_3CHO. Comparison of the *ldep* (solid line) and *udep* (dashed line) scenarios shows that more rapid deposition strengthened the CF_3CHO diel variability. In contrast to its precursors, HFC-23 continued to accumulate throughout the simulation (Fig. 6c), consistent with its long atmospheric lifetime, following linear growth once CF_3CHO reached steady state.

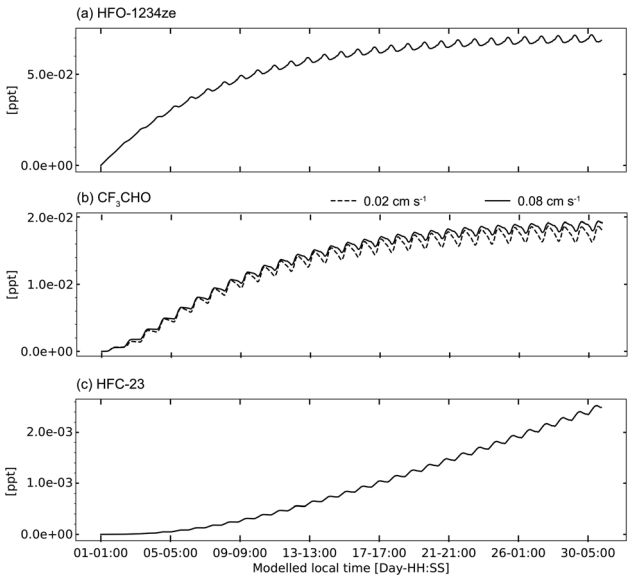

Fig. 6 Modelled mixing ratios of (a) HFO-1234ze, (b) CF_3CHO and (c) HFC-23 from the *G15_lqy* scenarios. Panel (b) also compares the results from the *G15_lqy_ldep* (solid) and *G15_lqy_udep* (dashed) scenarios (see Table 3 for scenario definitions).

The final mixing ratios of HFO-1234ze, CF_3CHO and HFC-23 for each modelled scenario are summarized in Table 4. The HFO-1234ze mixing ratios modelled using the 2015 global scenarios (*G15*), considered here as background values, stabilized at 69 ppq for the last 10 simulation days. Using the 2015 China emission scenarios (*C15*), the HFO-1234ze mixing ratios stabilized at 3610 ppq. We compare these values to those reported by Wang *et al.*[1] from simulations using the same 2015 emissions as input to a global 3-D chemical transport model (GEOS-Chem). Wang *et al.*[1] reported average annual mixing ratios in background areas of 55 ppq, with average summer values over China of 7230 ppq. This comparison shows that the HFO-1234ze predictions from the two models agree to within a factor of two, despite significant differences between the two model set-ups and assumptions.

The differences in HFO-1234ze between the two models propagated to CF_3CHO. In addition, we included two CF_3CHO removal processes (photolysis and deposition) that were not considered by Wang *et al.*,[1] and so our CF_3CHO mixing ratios are expectedly lower. In our global (background) simulations (*G15*), final CF_3CHO mixing ratios were 16–19 ppq, compared to background values from Wang *et al.*[1] of 60 ppq. In our China simulations (*C15*), final CF_3CHO was between 650 and 1010 ppq, a factor of 3–4 lower than the 2720 ppq reported Wang *et al.*[1] for China in summer. Give the importance of both photolysis and deposition to CF_3CHO removal shown in Section 3.1, we expect that CF_3CHO was significantly overestimated in the 3-D simulations of Wang *et al.*[1] that neglected these processes.

The 2050 values of all modelled species increased by a factor of 9.8 relative to the 2015 simulations (Table 4). This result was consistent with the results from the 3-D model[1] and was driven by the linearity in the projected emissions (from Wang *et al.*[1]) and the fact that we maintained the same atmospheric and meteorological conditions between the 2015 and 2050 scenarios.

Table 4 Final modelled mixing ratios (ppq) of HFO-1234ze, CF_3CHO and HFC-23 in each scenario

Scenario ID	HFO-1234ze	CF_3CHO	HFC-23
G15_lqy_ldep	69	19.2	2.6
G15_lqy_udep	69	16.6	2.3
G15_uqy_ldep	69	18.6	8.7
G15_uqy_udep	69	16.1	7.6
C15_lqy_ldep	3610	1010	137
C15_uqy_udep	3610	652	307
G50_lqy_ldep	677	189	25.6
G50_lqy_udep	677	164	22.2
G50_uqy_ldep	677	183	86
G50_uqy_udep	677	159	74.8
C50_lqy_ldep	35 500	9900	1350
C50_uqy_udep	35 500	6420	3020

Table 5 Projected HFC-23 growth rate and percentage contribution to the current HFC-23 growth rate (1 ppt per year) from HFC-23 produced from HFO-1234ze *via* CF_3CHO photolysis[a]

Scenario ID	HFC-23[b] [ppt per yr]	Contribution to current HFC-23 growth rate[c] [%]
G15_lqy_udep	0.038	3.8
G15_lqy_ldep	0.044	4.4
G15_uqy_udep	0.126	12.6
G15_uqy_ldep	0.147	14.7
G50_lqy_udep	0.370	—
G50_lqy_ldep	0.432	—
G50_uqy_udep	1.244	—
G50_uqy_ldep	1.445	—

[a] The scenarios are organized from lowest to highest growth rates. [b] Extrapolated to annual as described in the text. [c] Present-day growth rate not applicable for 2050 scenarios.

3.3 HFC-23 produced from HFO-1234ze through CF_3CHO photolysis: implications for climate forcing

Table 4 shows that after just 30 days of simulation using 2015 emissions, HFC-23 mixing ratios reached values of 2–9 ppq in the global background scenarios (*G15*) and up to 300 ppq in the China scenarios (*C15*). We used our simulations to contextualize the possible production of HFC-23 from HFO-1234ze (*via* CF_3CHO) against the measured current HFC-23 annual growth rate of 1 ppt per year.[16] As the precursor species reached steady state after ~15–20 days, we used the HFC-23 output from the final 10 days of the simulations to calculate the average daily HFC-23 growth rate (ppt per day) and projected the estimated growth rate to a yearly value. Our projection assumes HFC-23 will continue to grow linearly throughout the year, an assumption we consider reasonable given the long HFC-23 lifetime.

Table 5 shows the growth rate (ppt per yr) of HFC-23 from HFO-1234ze emissions, along with the implied percentage contribution of this source to the observed present-day HFC-23 growth rate of 1 ppt per year. The table shows that the HFC-23 produced from the HFO-1234ze–CF_3CHO photochemical cascade could be responsible for between 3.8% and 14.7% of current HFC-23 growth under the four *G15* scenarios. Using the most likely scenario of low V_{dep}, low ϕ_2 (*G15_lqy_ldep*), the potential contribution of 4.4% is small but not negligible. As discussed above, the HFC-23 yield scales with quantum yield, so future estimates of quantum yield can be used to amend this contribution to HFC-23 growth.

Emissions of HFO-1234ze are projected to increase by nearly a factor of 10 by 2050,[1] with commensurate increases in HFC-23 mixing ratios as shown in Table 4. The estimates in this work considered only one CF_3CHO precursor: HFO-1234ze. The aggregated impact of the CF_3CHO photolysis to HFC-23 from other sources (*i.e.*, other species that degrade in the atmosphere to CF_3CHO) requires these other sources also to be modelled.

4 Summary and conclusions

In this research, we modelled the atmospheric fate of CF_3CHO produced by HFO-1234ze using the box model AtChem2. We designed a set of modelling scenarios using the 2015 and 2050 HFO-1234ze emissions developed by Wang *et al.*[1]. Emissions were applied to model conditions representative of the global background planetary boundary layer and of China, where most the emissions of HFO-1234ze currently occur. We used real chemical and meteorological conditions from an urban atmosphere to constrain 30-day simulations for a northern hemisphere summer month. The reaction of HFO-1234ze with $OH^{\bullet}$ was configured as the only source for CF_3CHO.

Three atmospheric removal processes were explored for CF_3CHO: reaction with $OH^{\bullet}$, photolysis and deposition. For the photolysis, two channels were considered: the radical channel (eqn (1)) and the HFC-23 channel (eqn (2)). An overall quantum yield of 17% for CF_3CHO photolysis was used across all wavelengths. Two quantum yields for the HFC-23 channel were tested: $\phi_2 = 0.3\%$ and 1%. The remaining quantum yield was attributed to the radical channel, $\phi_1 = 16.7\%$ and 16.0%, respectively.

To determine the CF_3CHO deposition velocity, we used the GEOS-Chem 3-D model. We took advantage of the parameterization in the 3-D model to derive estimates for dry and wet deposition that were later implemented as deposition velocities V_{dep} (in cm s^{-1}) in AtChem2. We conducted experiments varying the H^{cp} between 0.96 M atm^{-1} (H^{cp} for CF_3CFO)[27] and 13.17 M atm^{-1} (H^{cp} for CH_3CHO), with the latter considered an unlikely upper value. Other unknown properties of CF_3CHO needed to determine its deposition (*e.g.*, $\frac{d \ln H^{cp}}{d(1/T)}, f_0$) were assumed using acetaldehyde values. The results from modelling the deposition of CF_3CHO in GEOS-Chem yielded three estimates for V_{dep}: 0.02 cm s^{-1}, 0.08 cm s^{-1} and 0.21 cm s^{-1} (with the former two based on global means and the latter based on the maximum value simulated in the 3-D model). We provided these bracketed V_{dep} estimates, inclusive of both dry and wet deposition, into our box model simulations. We consider that $V_{dep} = 0.02$ cm s^{-1} is the most reasonable of the values tested.

Because of the unknown properties of CF_3CHO, we designed a series of 14 experiments to provide a range of estimates for its atmospheric fate and the uncertainty associated with the underlying parameters. These scenarios combined different atmospheric conditions (urban and pristine) and values for the HFC-23 channel ϕ_2 (0.3% and 1%), V_{dep} estimated with GEOS-Chem (0.02 cm s^{-1}, 0.08 cm s^{-1} and 0.21 cm s^{-1}), and 2015 and 2050 HFO-1234ze emissions for China and the globe. In all scenarios, HFO-1234ze and CF_3CHO reached steady state by the end of the 30-day modelling period, while HFC-23 increased continuously. The inclusion of CF_3CHO photolysis and deposition sinks in our simulations, not considered by Wang *et al.*,[1] led to lower CF_3CHO mixing ratios than the Wang *et al.*[1] estimates.

We found that the simulations were most sensitive to the choice of quantum yield, with a 3-fold difference in ϕ_2 translating to an equivalent difference in HFC-23 mixing ratios. Meanwhile, the 4-fold difference in V_{dep} in our global scenarios resulted in only a ~20% difference in HFC-23, and the difference between urban and pristine conditions was negligible. These results point to the quantum yield as the most critical

uncertainty to reduce experimentally, followed by deposition parameters. When using the most plausible value for depositional losses ($V_{dep} = 0.02$ cm s^{-1}), the main loss mechanism of CF_3CHO was always photolysis, with the radical channel (eqn (1)) the dominant sink. Reaction with OH$^{\bullet}$ was next most important, followed by deposition. The HFC-23 photolysis channel accounted for between 1.3% (for $\phi_2 = 0.3\%$) and 4.4% (for $\phi_2 = 1\%$) of the CF_3CHO atmospheric removal globally, demonstrating a linear response between ϕ_2 and HFC-23 production (and between their uncertainties).

These results assume all HFO-1234ze reacts within the planetary boundary layer. However, recent work has demonstrated that ϕ_2 is pressure dependent, increasing for lower pressures.[3] Since the HFO-1234ze lifetime is ~16 days, it can be transported to the upper troposphere where the lower pressures may imply a higher ϕ_2. While Wang *et al.*[1] suggested that the chemistry of HFO-1234ze is localised, transport of this substance beyond the planetary boundary layer must be considered. Furthermore, the effect of the CF_3CHO deposition would be substantially reduced in the free troposphere, thus changing the proposed CF_3CHO sink distribution and increasing the importance of the photochemical sinks. Under free tropospheric conditions, we therefore anticipate a larger yield of HFC-23 from HFO-1234ze.

Using 2015 HFO-1234ze emissions, we estimated final HFC-23 mixing ratios after 30 days of simulation of 2.3–8.7 ppq in the global background and 0.14–0.31 ppt over an area representative of China. Recent atmospheric observations show that the annual growth rate of HFC-23 is ~1 ppt per year.[16] Using four 2015 global scenarios, we find that the HFC-23 photolysis channel of CF_3CHO produced from HFO-1234ze could account for ~4–15% of the current HFC-23 global growth rate, with the most likely scenarios at the lower end of this range.

Our simulations showed that by 2050, all modelled species increased by a factor of 9.8 compared to their 2015 values. This trend in mixing ratio implies a linear response of both CF_3CHO and HFC-23 to HFO-1234ze emissions. We find that under projected 2050 emissions increases, the annual growth rate of HFC-23 from HFO-1234ze degradation chemistry alone could be as high as 1.4 ppt per year, almost 50% larger than the present-day increase from all sources. While the more likely scenarios imply a lower HFC-23 growth rate of ~0.4 ppt per year, the simulated magnitude of future HFC-23 production is a cause for concern. Here we have considered only one of the HFOs known to produce CF_3CHO,[10,11] and by extension, HFC-23; however, emissions of other CF_3CHO-producing HFOs are also projected to grow substantially in the coming decades.[34] Our results imply a potential need to reconsider the labelling of HFOs as "low-GWP" alternatives, with more precise quantification of the HFC-23 quantum yield from CF_3CHO critical for understanding the true climate impact of HFO use.

Author contributions

MPPP performed all the simulations and data analysis. CH, SHK and JAF conceived the project. SHK and JAF directed the project. All authors contributed to the drafting of the manuscript.

Conflicts of interest

There are no conflicts to declare.

Acknowledgements

The authors thank Professor Dylan Millet (University of Minnesota) for suggesting the use of GEOS-Chem to estimate dry deposition velocity for use in AtChem. This research was supported by the Australian Research Council (grants DP220102466 and DP220100891). The work was undertaken with the assistance of resources provided at the NCI National Facility systems at the Australian National University through the National Computational Merit Allocation Scheme supported by the Australian Government (projects m19, q90).

Notes and references

1 Y. Wang, Z. Wang, M. Sun, J. Guo and J. Zhang, *Sci. Total Environ.*, 2021, **780**, 146631.
2 M. P. Sulbaek Andersen and O. J. Nielsen, *Atmos. Environ.*, 2022, **272**, 118935.
3 J. Campbell, PhD thesis, UNSW, Sydney, 2022.
4 E. Granryd, *Int. J. Refrig.*, 2001, **24**, 15–24.
5 J. M. Calm, *Int. J. Refrig.*, 2008, **31**, 1123–1133.
6 M. O. McLinden and M. L. Huber, *J. Chem. Eng. Data*, 2020, **65**, 4176–4193.
7 J. S. Park, H. T. Kim, J. D. Kim, J. H. Kim, S. K. Kim and J. M. Lee, *J. Appl. Polym. Sci.*, 2022, **139**, 397.
8 S. Henne, D. E. Shallcross, S. Reimann, P. Xiao, D. Brunner, S. O'Doherty and B. Buchmann, *Environ. Sci. Technol.*, 2012, **46**, 1650–1658.
9 M. S. Javadi, R. Søndergaard, O. J. Nielsen, M. D. Hurley and T. J. Wallington, *Atmos. Chem. Phys.*, 2008, **8**, 3141–3147.
10 M. Baasandorj, A. R. Ravishankara and J. B. Burkholder, *J. Phys. Chem. A*, 2011, **115**, 10539–10549.
11 M. P. Sulbaek Andersen, J. A. Schmidt, A. Volkova and D. J. Wuebbles, *Atmos. Environ.*, 2018, **179**, 250–259.
12 M. Scheurer, K. Noedler, F. Freeling, J. Janda, O. Happel, M. Riegel, U. Müller, F. R. Storck, M. Fleig, F. T. Lange, A. Brunsch and H.-J. Brauch, *Water Res.*, 2017, **126**, 460–471.
13 K. M. Stanley, D. Say, J. Muhle, C. M. Harth, P. B. Krummel, D. Young, S. J. O'Doherty, P. K. Salameh, P. G. Simmonds, R. F. Weiss, R. G. Prinn, P. J. Fraser and M. Rigby, *Nat. Commun.*, 2020, **11**, 397.
14 G. Cisse, R. McLeman, H. Adams, P. Aldunce, K. Bowen, D. Campbell-Lendrum, S. Clayton, K. L. Ebi, J. Hess, C. Huang, Q. Liu, G. McGregor, J. Semenza and M. C. Tirado, *Climate Change 2022: Impacts, Adaptation and Vulnerability, Contribution of Working Group II to the Sixth Assessment Report of the Intergovernmental Panel on Climate Change*, ed. H.-O. Pörtner, D. C. Roberts, M. Tignor, E. S. Poloczanska, K. Mintenbeck, A. Alegría, M. Craig, S. Langsdorf, S. Löschke, V. Möller, A. Okem and B. Rama, Cambridge University Press, Cambridge, UK and New York, NY, USA, pp. 1041–1170, DOI: 10.1017/9781009325844.009.

15 A. M. Fernando, P. F. Bernath and C. D. Boone, *J. Quant. Spectrosc. Radiat. Transfer*, 2019, **238**, 106540.
16 P. G. Simmonds, M. Rigby, A. McCulloch, M. K. Vollmer, S. Henne, J. Muhle, S. O'Doherty, A. J. Manning, P. B. Krummel, P. J. Fraser, D. Young, R. F. Weiss, P. K. Salameh, C. M. Harth, S. Reimann, C. M. Trudinger, L. Paul S, R. H. Wang, D. J. Ivy, R. G. Prinn, B. Mitrevski and D. M. Etheridge, *Atmos. Chem. Phys.*, 2018, **18**, 4153–4169.
17 M. Chiappero, F. Malanca, G. Arguello, D. Wooldridge, M. Hurley, J. Ball, T. Wallington, R. Waterland and R. Buck, *J. Phys. Chem.*, 2006, **110**, 11944–11953.
18 A. Rickard, *The MCM Project*, 2021, **http://mcm.york.ac.uk/project.htt**.
19 M. E. Jenkin, S. M. Saunders, V. Wagner and M. J. Pilling, *Atmos. Chem. Phys.*, 2003, **3**, 181–193.
20 S. P. Sander, R. R. Friedl, D. M. Golden, M. J. Kurylo, G. K. Moortgat, P. H. Wine, a. R. Ravishankara, C. E. Kolb, M. J. Molina, S. Diego, L. Jolla, R. E. Huie and V. L. Orkin, *Chemical Kinetics and Photochemical Data for Use in Atmospheric Studies Evaluation Number 15*, 2020, **http://jpldataeval.jpl.nasa.gov/**.
21 S. R. Sellevag, T. Kelly, H. Sidebottom and C. J. Nielsen, *Phys. Chem. Chem. Phys.*, 2004, **6**, 1243–1252.
22 J. Petterson, *Calculated Actinic Fluxes (290 – 700 Nm) for Air Pollution Photochemistry Applications, U.S. Environmental Protection Agency Technical Report*, 1976.
23 J. H. Seinfeld and S. N. Pandis, *Atmospheric Chemistry and Physics. From Air Pollution to Climate Change*, John Wiley & Sons, Inc., 3rd edn, 2016, pp. 1031–1046.
24 M. Wesely, *Atmos. Environ.*, 1988, **23**, 1293–1304.
25 P. H. Wine and W. L. Chameides, *Report Number: Global Ozone Research and Monitoring Project – Report No. 20: Possible Atmospheric Lifetimes and Chemical Reaction Mechanisms for selected HCFCs, HFCs, CH_3CCl_3, and Their Degradation Products against Dissolutionand/or Degradation in Seawater and Cloud Water, Georgia Tech Research Institute and School of Geophysical Sciences Technical Report*, 1989.
26 E. A. Betterton and M. R. Hoffmann, *Environ. Sci. Technol.*, 1988, **22**, 1415–1418.
27 J. B. Burkholder, R. A. Cox and A. R. Ravishankara, *Chem. Rev.*, 2015, **115**, 3704–3759.
28 W. J. de Bruyn, J. A. Shorter, P. Davidovits, D. R. Worsnop, M. S. Zahniser and C. E. Kolb, *Environ. Sci. Technol.*, 1995, **29**, 1179–1185.
29 H. Liu, D. J. Jacob, I. Bey and R. M. Yantosca, *J. Geophys. Res.*, 2001, **106**, 12109–12128.
30 R. Sander, *Atmos. Chem. Phys.*, 2015, **15**, 4399–4981.
31 D. B. Millet, A. Guenther, D. A. Siegel, N. B. Nelson, H. B. Singh, J. A. D. Gouw, C. Warneke and J. Williams, *Atmos. Chem. Phys. Discuss.*, 2009, **9**, 24225–24279.
32 L. K. Whalley, K. L. Furneaux, A. Goddard, J. D. Lee, A. Mahajan, H. Oetjen, K. A. Read, N. Kaaden, L. J. Carpenter, A. C. Lewis, J. M. C. Plane, E. S. Saltzman, A. Wiedensohler and D. E. Heard, *Atmos. Chem. Phys.*, 2010, **10**, 1555–1576.
33 S. I. Bohnenstengel, S. E. Belcher, A. Aiken, J. D. Allan, G. Allen, A. Bacak, T. J. Bannan, J. F. Barlow, D. C. Beddddows, W. J. Blossss, A. M. Booth, C. Chemel, O. Coceal, C. F. Di Marco, M. K. Dubey, K. H. Faloon, Z. L. Flemiming, M. Furger, J. K. Gietl, R. R. Graves, D. C. Green, C. S. Grimmimmimmond, C. H. Halios, J. F. Hamiamiamilton, R. M. Harrisison, M. R. Heal, D. E. Heard, C. Helfter, S. C. Herndon, R. E. Holmes, J. R. Hopkins, A. M. Jones, F. J. Kelly, S. Kotthaus, B. Langford, J. D. Lee, R. J. Leigh, A. C. Lewisis, R. T. Lidsidsidster, F. D. Lopez-Hilfiker, J. B. McQuaidaid, C. Mohr, P. S. Monks, E. Nemimitz, N. L. Ng, C. J. Percival, A. S. Prevot, H. M. Ricketts, R. Sokhi, D. Stone, J. A. Thornton, A. H. Tremper, A. C. Valach, S. Vississsisser, L. K. Whalley, L. R. Williamsiamsiamsiams, L. Xu, D. E. Young and P. Zotter, *Bull. Am. Meteorol. Soc.*, 2015, **96**, 779–804.
34 Y. Wang, L. Liu, X. Qiao, M. Sun, J. Guo, J. Zhang and B. Zhao, *Environ. Sci. Technol.*, 2023, **57**, 8650–8659.